Dislocated vector asymmetric soliton molecules in birefringence-managed fiber lasers

Zhiwen He ⓘ, Yueqing Du, Yufeng Zhang, Qun Gao, Chao Zeng, Dong Mao ⓘ,* and Jianlin Zhao ⓘ

Key Laboratory of Light Field Manipulation and Information Acquisition, Ministry of Industry and Information Technology,
Shaanxi Key Laboratory of Optical Information Technology, and School of Physical Science and Technology,
Northwestern Polytechnical University, Xi'an 710072, China

Optical soliton molecules, the self-organized structures in dissipative systems arising from the equilibrium between attractive and repulsive forces, show great importance for revealing soliton interactions and potential applications in optical communications. Here, we numerically and experimentally demonstrate that two orthogonally polarized components with mirrored profiles can form vector soliton molecules in single-mode fiber lasers containing a section of polarization-maintaining fiber. Due to the dynamic balance between fiber birefringence and chromatic dispersion, the temporal dislocation between two components changes along the cavity while reaching the self-consistent state per round trip. The unequal coupling for orthogonally polarized modes at the input interface of the polarization-maintaining fiber dominates the asymmetric property of subpulses for each component. Such soliton molecules are observed both in erbium-doped and ytterbium-doped fiber lasers, indicating the generality of the vector asymmetric structures. Our work reveals soliton molecules with additional degrees of freedom in polarization and intensity, expanding the understanding of the asymmetric mode interactions in fiber lasers.

I. INTRODUCTION

Solitons, the self-organized localized structures capable of propagating a long distance without distortion, have attracted considerable interest in various fields of science, ranging from Bose-Einstein condensation [1] to plasma [2], hydrodynamics [3], and nonlinear optics [4]. In optics, ultrafast fiber lasers serve as reliable dissipative testbeds for exploring the fantastic dynamics of solitons [5,6]. At high pumping levels, due to strong nonlinearity such as the peak-power-clamping effect, nonlinear phase shift, and gain saturation [7,8], mode-locked fiber lasers are prone to operate in multipulse regimes, which can regulate into diverse multiple soliton patterns such as soliton rains [9], soliton bunches [10], harmonic mode-locking solitons [11], and soliton molecules (SMs, also known as bound-state solitons) [12,13]. Generally, SMs are composed of two or multiple solitons with specific phase difference and temporal separation, possessing great potential in enhancing the data-carrying capacity of optical communications [12]. Since the first prediction of SMs proposed by Malomed in 1991 [14] and further numerical demonstration by Akhmediev *et al.* in 1997 [15], SMs have been broadly researched in diverse nonlinear systems, e.g., breathing SMs [16] and vector SMs [17,18] in fiber lasers and dark SMs in superfluid [19], as well as heteronuclear SMs in microresonators [20].

On a different note, solitons in fiber lasers are firstly treated as scalar structures, despite single-mode fiber (SMF) supporting two orthogonally polarized modes [21,22]. The vector nature of solitons was first illustrated by Menyuk in 1987 [23], where the group velocity difference of two orthogonally polar-

ized modes can be compensated by inverse central frequency shift. Naturally, the SM also owns the degree of freedom in the polarization. In recent decades, polarization-locked SMs, group-velocity-locked SMs, and polarization-rotation SMs [24,25] have been observed in fiber lasers by tailoring the cavity birefringence and the coupling strength between two orthogonally polarized components. Besides, due to the soliton-energy-quantization effect (the gain competition among multisolitons) [8], subpulses in SMs usually have identical amplitudes and durations [26–28], i.e., symmetric SMs.

Noting that solitons with distinct characteristics may coexist when symmetry breaking among different polarization modes occurs, corresponding studies have greatly expanded the knowledge of intriguing nonlinear dynamics in optical cavities [29–31]. Recently, the symmetry breaking of both polarization and temporal profiles has been observed for the largely separated trisolitons in a driven Kerr resonator [32]. In the frame of fiber lasers, though asymmetric SMs exhibiting complex internal pulsations have been observed [24,33,34], most of these studies focused on the anomalous-dispersion regime and the corresponding formation mechanism remains unclear. Intuitively, it is meaningful to explore unique types of asymmetric SMs in normal-dispersion fiber lasers and unveil their formation mechanism, which may significantly promote the understanding of asymmetric mode interactions in fiber lasers.

Here, we demonstrate that two temporally dislocated orthogonally polarized asymmetric SMs can assemble what we define as the dislocated vector asymmetric soliton molecule (DVASM) by incorporating a section of polarization-maintaining fiber (PMF) into the SMF laser. The observations of dual-pulse or tri-pulse DVASM in erbium-doped fiber (EDF) lasers and DVASM in ytterbium-doped fiber (YDF)
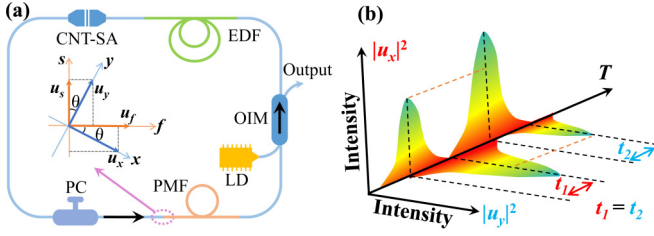
*maodong@nwpu.edu.cn

FIG. 1. Experiment setup and sketch of the DVASM. (a) Configuration of the SMF laser with a section of PMF. (b) Properties of the DVASM, in which two orthogonally polarized components are dislocated in the temporal domain, and each of them consists of unequal subpulses. LD, laser diode; OIM, optical integrated module, a combiner of the wavelength division multiplexer, the output coupler, and the polarization-independent isolator; EDF, erbium-doped fiber; CNT-SA, carbon nanotube saturable absorber; PC, polarization controller; PMF, polarization-maintaining fiber.

lasers corroborate the universality of such SM. The numerical simulation well reproduces the experimental result, confirming that the DVASM is fundamentally different from other vector solitons or SMs. It is demonstrated that the dynamic balance between the strong birefringence and dispersion gives rise to the peculiar temporal dislocation between orthogonally polarized components, while the PMF-induced unequal mode coupling contributes to the asymmetric subpulses in each component.

II. EXPERIMENTAL SETUP

Figure 1(a) illustrates the sketch of the fiber laser, in which the 976-nm laser diode pumps 7.2-m EDF (EDFC-980-HP) through an optical integrated module (OIM) including the wavelength division multiplexer, the polarization-independent isolator, and the output coupler with 30% output ratio. A carbon nanotube saturable absorber (CNTSA) enables the passive mode locking. The 1-m PMF (PM1550-HP) introduces large birefringence to the cavity, while the polarization controller adjusts the orientation angle of the light before PMF. All the pigtails of the fiber components are SMF (SMF-28e+) with a total length of 1 m. The dispersion parameters D of the SMF, EDF, and PMF are 17, −16.5, and 17 ps/(nm km) respectively; therefore the net cavity dispersion is calculated as ∼0.11 ps², confirming that the fiber laser operates in the normal-dispersion regime. The output pulses are characterized by an optical spectrum analyzer, a frequency-resolved optical gating (FROG), an autocorrelator, an oscilloscope, and a radio-frequency spectrum analyzer.

III. SIMULATION MODEL

Based on the coupled Ginzburg-Landau equations that incorporate birefringence, nonlinearity, dispersion, gain, and loss [7], we performed numerical simulation to reveal the formation mechanism of the pulse inside the fiber laser:

$$
\frac{\partial u_x}{\partial z} = -i\beta u_x + \delta \frac{\partial u_x}{\partial t} - i\frac{k_2}{2}\frac{\partial^2 u_x}{\partial t^2} + i\gamma\left(|u_x|^2 + \frac{2}{3}|u_y|^2\right)u_x
$$
$$
+ \frac{i\gamma u_y^2 u_x^*}{3} + \frac{(g-\alpha)}{2}u_x + \frac{g}{2\Omega_g^2}\frac{\partial^2 u_x}{\partial t^2}
$$

$$
\frac{\partial u_y}{\partial z} = i\beta u_y - \delta \frac{\partial u_y}{\partial t} - i\frac{k_2}{2}\frac{\partial^2 u_y}{\partial t^2} + i\gamma\left(|u_y|^2 + \frac{2}{3}|u_x|^2\right)u_y
$$
$$
+ \frac{i\gamma u_x^2 u_y^*}{3} + \frac{(g-\alpha)}{2}u_y + \frac{g}{2\Omega_g^2}\frac{\partial^2 u_y}{\partial t^2}. \qquad (1)
$$

Here, u_x and u_y are envelopes of two orthogonally polarized components, respectively. t corresponds to retarded time and z relates to the cavity position. Δn, $2\beta = 2\pi \Delta n/\lambda$, and $2\delta = 2\beta\lambda/2\pi c$ are the differences in the refractive indices, wave number, and inverse group velocity between u_x and u_y components, respectively. k^2 is the dispersion coefficient, α represents the loss, and γ is the fiber nonlinear coefficient. $g = g_0\exp(-E_p/E_s)$ is the saturable gain and Ω_g corresponds to the gain bandwidth, where E_p, g_0, and E_s relate to the pulse energy, small-signal gain coefficient, and gain saturation energy, respectively. The CNTSA is modeled by $T = 0.43 - T_0/[1 + P_{(\tau)}/P_{sat}]$, where T_0 is the modulation depth, $P_{(\tau)}$ is the instantaneous power, and P_{sat} is the saturation power. The simulation parameters are set as follows to match the experimental condition: $\lambda = 1560$ nm, $\Omega_g = 25$ nm, $g_0 = 0.7\,\mathrm{m}^{-1}$, $T_0 = 7\%$, $P_{sat} = 8$ W. For the 7.2-m EDF, $\gamma = 3\,\mathrm{W}^{-1}\,\mathrm{km}^{-1}$, $\Delta n = 1.5 \times 10^{-6}$, and $\beta_2 = 21.30\,\mathrm{ps}^2\,\mathrm{km}^{-1}$, while for the 1-m SMF, $\gamma = 1\,\mathrm{W}^{-1}\,\mathrm{km}^{-1}$, $\Delta n = 1.5 \times 10^{-6}$, and $\beta_2 = -21.95\,\mathrm{ps}^2\,\mathrm{km}^{-1}$. For the 1-m PMF, $\Delta n = 3.6 \times 10^{-4}$ and other parameters are the same as that of the SMF.

Different from standard fiber lasers, the mode coupling should be particularly considered at the interface from SMF to PMF inside the cavity. The coupling depends on the polarization orientation angle θ in Fig. 1(a), which can be expressed as

$$
[u_f \ u_s] = [u_x \ u_y]\begin{bmatrix} \cos\theta & -\sin\theta \\ \sin\theta & \cos\theta \end{bmatrix}. \qquad (2)
$$

Here the u_x and u_y denote the fast and slow components along the low-birefringent SMF, while the slow and fast components along high-birefringent PMF are represented by u_s and u_f, respectively. At the terminal of the PMF, θ is set as 0 so that the u_s (u_f) component in PMF transforms into the u_y (u_x) component in SMF.

The above mode coupling results depend on the orientation angle θ, which may result in the unequal amplitudes of subpulses for each orthogonally polarized component. With two identical initial pulses, the pulse profile for each component after mode coupling rests with the angle θ, as displayed in Figs. 2(a) and 2(b). For θ of 0.25π, both the u_s and u_f components evolve to soliton pairs composed of two equal subpulses [Fig. 2(c)]. Nonetheless, when θ deviates from 0.25π [e.g., 0.34π in Fig. 2(d)], the subpulses in each component have unequal amplitudes. Therefore, due to the repeated unequal mode coupling, such fiber laser is prone to reach a self-consistent state where two components comprise distinct subpulses.

IV. RESULTS

A. Measured and simulated DVASM in EDF laser

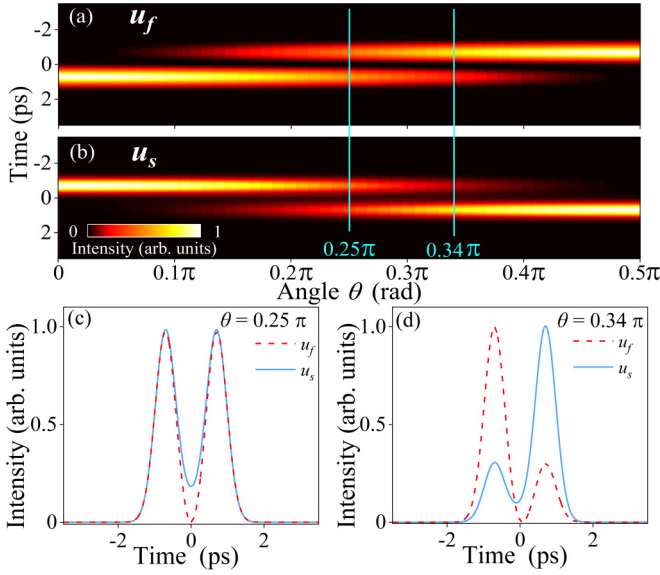The operation of the normal-dispersion birefringence-managed fiber laser rests with the polarization orientation θ;

FIG. 2. Origination of the unequal subpulses of each orthogonally polarized component in DVASM. Temporal profiles of the (a) u_f and (b) u_s components versus the polarization orientation angle θ. Concrete pulse profiles for the condition of (c) $\theta = 0.25\pi$ and (d) $\theta = 0.34\pi$, the u_f and u_s are denoted by red (short dash) and blue (solid) curves.
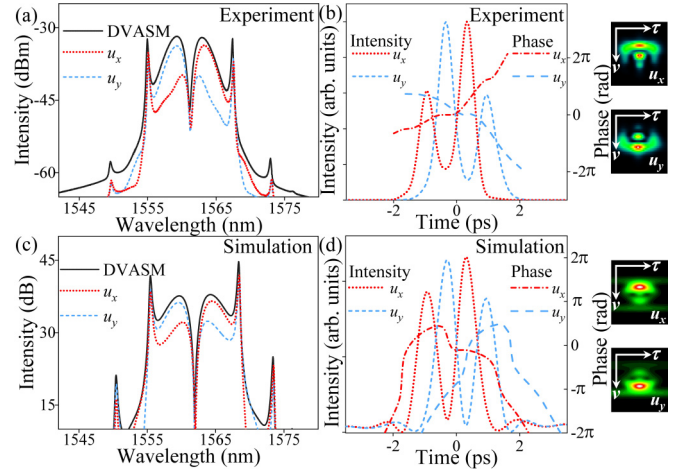

FIG. 3. Properties of the dual-pulse DVASM. Experimental results: (a) spectra, (b) retrieved FROG traces, pulse profiles, and phases. Simulation results: (c) spectra, (d) spectrograms, pulse profiles, and phases. The spectra of the DVASM, and the u_x and u_y components are denoted by black (solid), red (short dot), and blue (short dash) curves, respectively. The temporal intensities of the u_x and u_y components are represented by red (short dot) and blue (short dash) curves, while the phases of u_x and u_y are delineated by red (short dash dot) and blue (dash) curves, respectively.

for example, a single giant-chirp dissipative soliton and chirp-free birefringence-managed soliton (BMS) can be achieved for θ of $\pi/2$ and $\pi/4$, respectively [35]. Here, we mainly focused on the DVASM composed of two orthogonally polarized asymmetric SMs. In the proposed fiber laser, single BMS and DVASM operations are obtained at the pump power of 14.5 and 15.6 mW, respectively. The output spectra, retrieved FROG traces, and pulse profiles of DVASM are shown in Figs. 3(a) and 3(b). Due to the birefringence-induced phase-matching effect [35,36], the spectrum exhibits pairs of resonant spectral peaks. Unlike the symmetric SMs with identical subpulses (see Appendix A), only a sharp dip locates on the spectral center, indicating constant destructive interference. After resolving the DVASM with a polarization beam splitter, the spectra of u_x and u_y components mirror each other at the spectral center, and each of them consists of two unequal solitons. The corresponding autocorrelation traces are given in Appendix B, where for both components, their intensity ratios between the main peak and subpeak are larger than 2:1, also validating the unequal intensities of subpulses in DVASM. Noting that the weaker subpulse of DVASM is intrinsically distinct from the small temporal oscillating tail of BMS, which is caused by spectral sideband interference; similar structures have been observed in conventional solitons [37–39]. During the whole experiment, the DVASM is quite stable and reproducible, as validated by the uniform oscilloscope traces and high signal-to-noise ratio on the radio-frequency spectra in Appendix C.

The simulation initiates from a low-intensity noise pulse; the dual-pulse DVASM can be obtained when θ ranges from 0.31π to 0.36π. Figures 3(c) and 3(d) show the typical DVASM for θ of 0.34π and E_s of 64 pJ, which consists of two orthogonally polarized components that manifest mirrored

profiles in both spectral and temporal domains. Coinciding with the pulse profiles retrieved from FROG traces in Fig. 3(b), the u_x and u_y components of the DVASM shown in Fig. 3(d) are both composed of unequal subpulses with $\sim$0.71 ps duration and $\sim$1.2 ps interseparation. The unequal amplitudes for subpulses of two components are ascribed to the unequal mode coupling at the input interface of PMF, as elaborated upon in Fig. 2. Additionally, the phase differences between the leading and trailing subpulses of the two components are irregular (0.21π for u_x and 0.77π for u_y), which is beyond the traditional theoretical description of SMs with the relative phase difference of an integer multiple of $\pi/2$ [13,40]. We note that there is a temporal dislocation of $\sim$0.61 ps between the stronger subpulses of the u_x and u_y components, which is also distinct from the group-velocity-locked vector solitons with an ignorable temporal dislocation [41].

B. Buildup dynamics of the DVASM

In our experiment, the dispersive Fourier transform (DFT) technique [33,42–45], which can map the spectral profiles into temporal waveforms (see details in Appendix D), is utilized to capture the buildup dynamics of the DVASM. For both the u_x and u_y components, a low-intensity noise pulse experiences several relaxation oscillations and gradually evolves to a metastable single-pulse state after $\sim$10 000 round trips (RTs). Under the combined actions of gain, dispersion, and nonlinear effects, the pulse grows quickly and splits into the transient soliton pairs from the $\sim$12 900th RT, as evidenced by the clear spectral interference patterns in Figs. 4(a) and 4(c), and the autocorrelation sidelobes in Figs. 4(b) and 4(d). The nascent pulse moves toward the dominant pulse until their separation reaches $\sim$1.2 ps at the $\sim$13 250th RT, and then two subpulses comove as a robust unit. Note that the subsequent
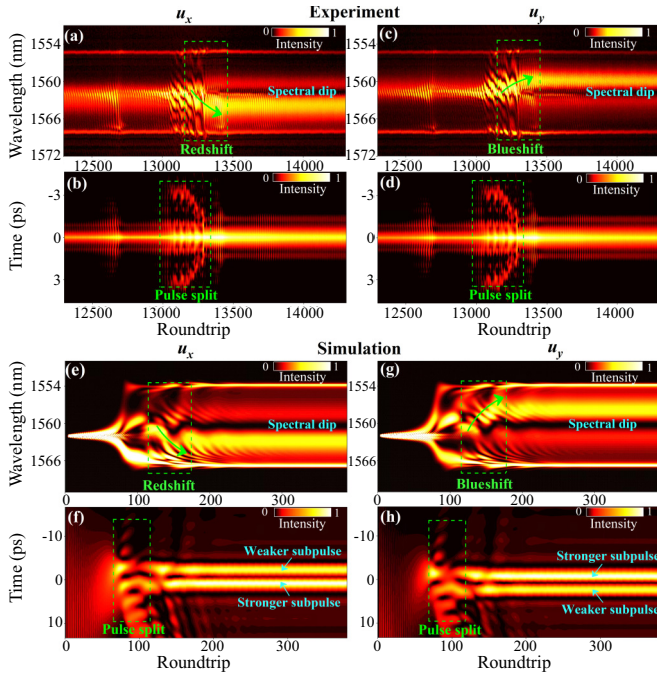
FIG. 4. Buildup processes of the dual-pulse DVASM. Top panel: (a) measured spectral and (b) field autocorrelation evolutions of the u_x component; (c) measured spectral and (d) field autocorrelation evolutions of the u_y component. Bottom panel: (e) simulated spectral and (f) temporal evolutions of the u_x component; (g) simulated spectral and (h) temporal evolutions of the u_y component.

evolutions of two components are mirrored to each other; for example, the majority of u_x (u_y) evolves to a longer (shorter) wavelength.

Based on the same simulation model, we numerically simulated the buildup process of the DVASM to further reveal its formation mechanism, as illustrated in the bottom panel of Fig. 4. At the first stage (0 to ~90 RTs), two components along the fast and slow axes evolve in a similar manner, e.g., the initial self-phase modulation-induced spectral broadening and subsequent spectral shaping into the one with several dips. In the time domain, the pulse intensity grows rapidly and starts to split into two asymmetric pulses at the 80th RT [Figs. 4(f) and 4(h)], which is ascribed to the combined effect of excessive nonlinear phase shift and the unequal mode coupling illustrated in Fig. 2. After that, two orthogonally polarized components evolve differently from 110 to ~300 RTs. For example, the cross-phase modulation shifts the centroid of the u_x spectrum to the longer wavelength while shifting that of the u_y spectrum to the shorter wavelength. As a result, each spectrum contains a main lobe and a secondary lobe with a dip on the center, corresponding to two unequal subpulses formed in the time domain. For the u_x component, its leading subpulse is weaker than the trailing one, while the u_y component behaves oppositely. Finally, both components realize the self-consistent state, and stable DVASM operation is achieved. Both experimental and simulation results indicate that the buildup of DVASM includes the centroid shift of the spectrum and the formation of unequal pulses.
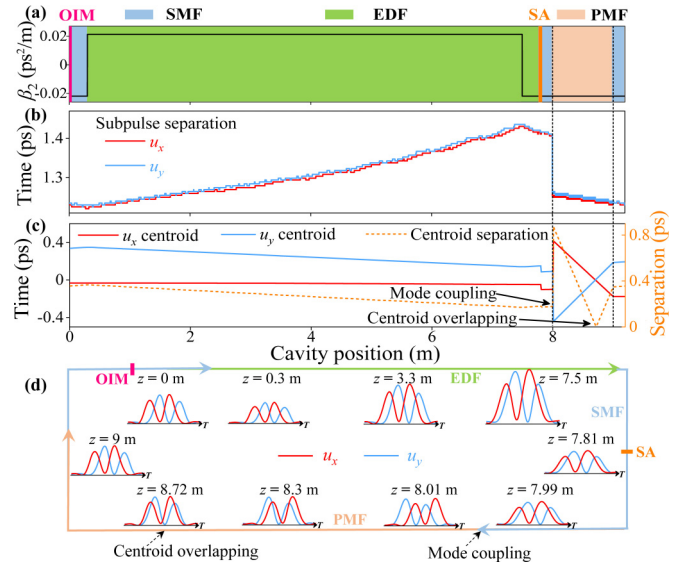

FIG. 5. Intracavity evolution of the dual-pulse DVASM. (a) Laser loop and fiber dispersion parameters along the cavity. (b) Intersubpulse separations and (c) temporal centroids of each component versus cavity position. (d) Sketch of temporal profile evolutions for u_x (red) and u_y (blue) components along the cavity, where z represents the cavity location.

C. Intracavity evolution of the DVASM

The intracavity evolutions for the dual-pulse DVASM are further investigated to ascertain the mechanism of self-consistent propagation in the fiber laser. Figure 5(a) illustrates the arrangement of laser components and fiber dispersion parameters, where the OIM is set as the start point for clear description. Figure 5(b) displays the subpulse separation of each polarization component, and the separation between subpulses increases in the normal-dispersion EDF. After being compensated slightly by the SMF, the separation decreases abruptly at the input terminal of PMF due to the mode coupling described by Eq. (2). During the whole evolution, the intersubpulse separation is always larger than 1.2 ps.

The centroid separation between two components is plotted in Fig. 5(c). Before entering the PMF, the temporal centroid of the u_y lags behind that of u_x due to the small birefringence of the EDF and SMF. At the input terminal of the PMF, mode coupling occurs and the temporal centroid of u_y is shifted ahead of that of u_x. Due to the strong birefringence of the PMF, the two orthogonally polarized components gradually approach each other, and the separation between their temporal centroids decreases linearly. The centroids of two components overlap at the cavity position of 8.72 m (i.e., the latter half part of the PMF), as marked in Fig. 5(c). The overlapping point deviates from the PMF center (cavity position of 8.5 m), which partially counteracts the group delay difference induced by chromatic dispersion. After the overlapping, two components continue departing from each other during propagation through the rest of the PMF. It is indicated that the birefringence of the fiber mainly compensates the abrupt temporal shift induced by the mode coupling of two components between the SMF and PMF, further ensuring the self-consistent intracavity evolution.
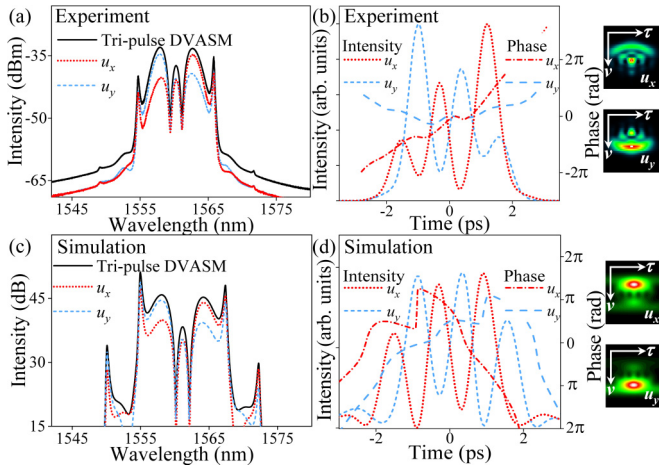
FIG. 6. Properties of the tri-pulse DVASM in the EDF laser. Experimental results: (a) spectra, (b) retrieved FROG traces, pulse profiles, and phases. Simulation results: (c) spectra, (d) spectrograms, pulse profiles, and phases. The spectra of the DVASM, and the u_x and u_y components are denoted by black (solid), red (short dot), and blue (short dash) curves, respectively. The temporal intensities of the u_x and u_y components are represented by red (short dot) and blue (short dash) curves, while the phases of u_x and u_y are delineated by red (short dash dot) and blue (dash) curves, respectively.
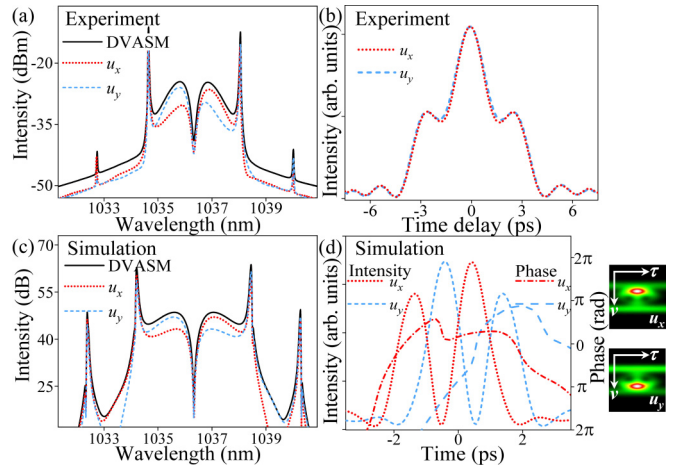
FIG. 7. Properties of the dual-pulse DVASM obtained in the YDF laser. Experimental results: (a) spectra, and (b) autocorrelation traces. Simulation results: (c) spectra, (d) spectrograms, pulse profiles, and phases. The spectra of the DVASM, and the u_x and u_y components are denoted by black (solid), red (short dot), and blue (short dash) curves, respectively. The temporal intensities of the u_x and u_y components are represented by red (short dot) and blue (short dash) curves, while the phases of u_x and u_y are delineated by red (short dash dot) and red (dash) curves, respectively.

Figure 5(d) manifests the temporal profiles of u_x (red curve) and u_y (blue curve) components at several typical positions, which validates the aforementioned analyses. Unlike traditional symmetric SMs whose coherent interseparation is realized by the interplay of repulsion and attraction related to their relative phase [12], for each orthogonally polarized component of the DVASM, the stability of the molecular structure is determined by the balance between the repulsion inside the normal-dispersion EDF and the overall attraction due to mode coupling at the input terminal of the PMF, in conjunction with the equilibrium between gain and loss. For the dynamic trapping between two components, the temporal dislocation results from the delicate equilibrium among birefringence-induced walk-off, mode-coupling-induced time shift, and chromatic-dispersion-induced group-velocity difference. Apparently, the mode coupling between the SMF and PMF plays an indispensable role in the formation of DVASM.

D. Tri-pulse DVASM in EDF laser and dual-pulse DVASM in YDF laser

Apart from the dual-pulse DVASM, the tri-pulse DVASM can also be experimentally observed by enhancing the pump power to 15.9 mW, as depicted in Figs. 6(a) and 6(b). Correspondingly, at the condition of $E_s = 88$ pJ and $\theta = 0.34\pi$, this type of DVASM can be reproduced in the simulation, as shown in Figs. 6(c) and 6(d). In the temporal domain, the two components are made up of three unequal subpulses that possess a similar pulse duration of ~0.73 ps and interseparation of ~1.2 ps, and there is also a temporal dislocation of ~0.61 ps between their adjacent subpulses. In the spectral domain, the spectral centroids of the u_x and u_y components are located at the longer and shorter wavelength regions, respectively, and a low-intensity hump exists around their

spectral center, which is also different from traditional SMs with equally spaced spectral interference fringes.

Interestingly, dual-pulse DVASM can also be obtained in an YDF laser containing a section of PMF, as illustrated in Figs. 7(a) and 7(b). For each component, there is a strong dip on the spectral center, and the autocorrelation trace indicates that each component of the DVASM is composed of two unequal subpulses, which is similar to that of DVASM formed in the EDF laser. Simulation results in Figs. 7(c) and 7(d) coincide with the experiment, and corresponding simulation parameters are expounded in detail in Appendix E. Therefore, DVASM is a ubiquitous soliton structure in birefringence-managed fiber lasers.

V. CONCLUSION AND PERSPECTIVE

In a birefringence-managed fiber laser, we experimentally and numerically demonstrate that two orthogonally polarized components, each consisting of two or three unequal subpulses, trap each other and form a vector soliton molecule with intriguing intracavity dynamics, namely, the DVASM. The distinct difference to the traditional vector SM is that the DVASM relies on the PMF-induced polarization mode coupling, while the traditional vector SM is, in the essence of the nonlinear modes trapping, ascribed to the Kerr effect (i.e., self-phase modulation, cross-phase modulation, and four-wave mixing). Unlike the previously reported symmetric SM, the subpulses of each DVASM component possess different amplitudes due to the unequal mode coupling between the SMF and PMF, which is a kind of explicit symmetry breaking caused by the intrinsic asymmetry of the nonlinear system.

There is an evident temporal dislocation between two components of the DVASM, which stems from the dynamic equilibrium of birefringence-induced walk-off, mode-coupling-
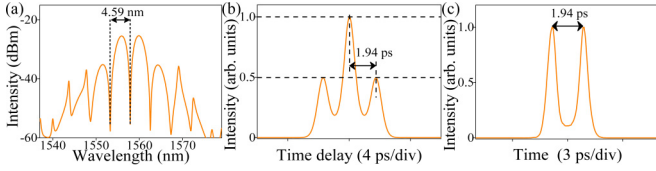
FIG. 8. Properties of a typical symmetric soliton molecule. (a) Spectrum, (b) autocorrelation trace, and (c) FROG retrieved pulse profile.

induced temporal shift, and group-velocity difference resulted from chromatic dispersion. DVASM can be observed both in EDF and YDF lasers, indicating that such pulse is a ubiquitous optical structure, resting with the birefringence management but independent of lasing wavelength. By further optimizing the laser parameters (e.g., a longer cavity length and stronger pump power), DVASM containing a larger number of solitons can be obtained, which is a promising pulse source for high-speed optical communications and a potential testbed for investigating vector soliton crystals.

Apart from the stationary SMs, oscillating or vibrating SMs [27,46,47] and breathing SMs [16] have drawn considerable interest in recent research. These dynamic optical structures arise from the Hopf bifurcation effect, and they can be utilized for all-optical switching [46]. Therefore, we anticipate that the dynamic DVASM can be an intriguing subject for further studying the Hopf bifurcation and interactions between orthogonally polarized nonlinear waves. Our results enlighten the understanding of explicit symmetry breaking in the bimodal systems, incentivizing further exploration for complicated optical structures with higher degrees of freedom, such as temporal dislocation, soliton number, polarization, and symmetry.

APPENDIX A: TYPICAL SYMMETRIC SOLITON MOLECULE

As displayed in Fig. 8(a), the spectrum of typical symmetric SMs manifests equally spaced spectral interference fringes. The intensity ratio of the subpeak to the center peak on the autocorrelation trace in Fig. 8(b) is ~0.5. Besides, the FROG retrieved pulse profile in Fig. 8(c) corroborates that this SM is composed of two equal solitons, which is totally different from each orthogonally polarized component of the DVASM.

APPENDIX B: AUTOCORRELATION TRACES OF DVASM

Autocorrelation traces for the two orthogonally polarized components of the DVASM are given in Fig. 9. It is evident that for both components, the intensity ratio of the subpeak
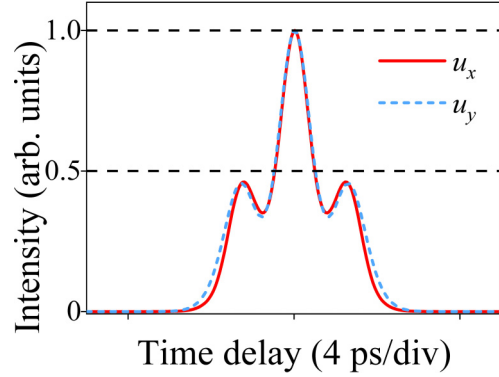

FIG. 9. Autocorrelation traces for the two components of the DVASM. The u_x and u_y components are denoted by red (solid) and blue (short dash) curves, respectively.

to the center peak is less than 0.5, further validating unequal amplitudes for two subpulses in each component.

APPENDIX C: OSCILLOSCOPE TRACES AND RADIO-FREQUENCY SPECTRA OF DVASM

As shown in Figs. 10(a) and 10(b), the u_x and u_y components of the DVASM possess the same pulse-pulse separation of ~44.6 ns and repetition rate of ~22.397 037 MHz, coinciding with the cavity length of ~9.2 m. In addition, the high signal-to-noise ratio (>50 dB) confirms the good stability of the laser.

APPENDIX D: IMPLEMENTATION FOR MEASURING REAL-TIME SPECTRA

We design a real-time spectrum measurement system to study the evolution of two orthogonally polarized components of the DVASM, as shown in Fig. 11. The laser is split to the u_x and u_y components by a polarization beam splitter outside the cavity. Especially, the u_x component propagates through an additional 4.5-m SMF; then the u_x component lags behind the u_y component after they are coupled into the SMF again. Hence, they are almost distributed with equal space in the time domain, even after being amplified by the erbium-doped fiber amplifier and temporally stretched by the 5000-m dispersion compensation fiber (DCF). Finally, pulse sequences are
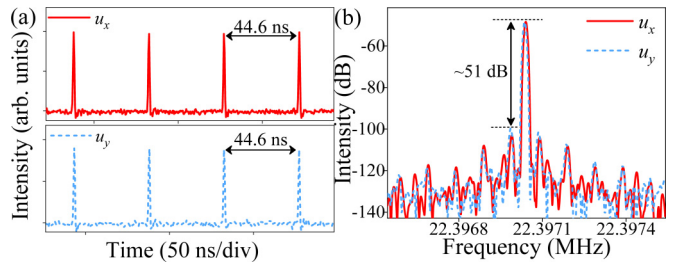

FIG. 10. (a) Oscilloscope traces and (b) radio-frequency spectra for the u_x and u_y components of the DVASM. u_x and u_y are denoted by red (solid) and blue (short dash) curves.
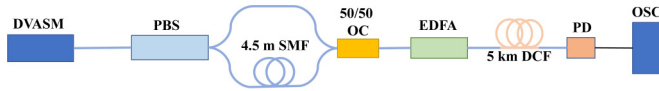
FIG. 11. The real-time spectra measurement setup. DVASM, dislocated vector asymmetric soliton molecule; PBS, polarization beam splitter; SMF, single-mode fiber; OC, optical coupler; EDFA, erbium-doped fiber amplifier; DCF, dispersion compensation fiber; PD, photodetector; OSC, oscilloscope.

converted to electrical signals by two photodetectors and captured by the oscilloscope.

As displayed in Figs. 12(a) and 12(b), after propagating through the 5000-m DCF, the sideband separations for the two orthogonally polarized components all reached ∼9.2 ns, coinciding well with the DFT mapping relation [42],

$$\Delta t = |D|L\Delta\lambda, \qquad (D1)$$

where Δt relates to the full width at half maximum of the broadened pulse, and $\Delta\lambda$ corresponds to the 3-dB bandwidth of the time-averaged spectrum. D [−150 ps/(nm km)] and L (5000 m) are the dispersion parameter and length of DCF, respectively. According to the final limitation of the DFT technique [42], the spectral resolution is calculated to be ∼0.33 nm. Besides, for both the u_x and u_y components, their single-shot spectra exhibit similar profiles to the time-averaged linear spectra, also verifying the reliability of the DFT measurement system.

APPENDIX E: SETUP AND SIMULATION PARAMETERS FOR THE YDF LASER

The YDF laser capable of achieving a DVASM has a similar ring configuration to that of the EDF laser, which is comprised of a wavelength division multiplexer, 1.25-m YDF (SM-YSF-HI), a 20:80 output coupler, 1.4-m PMF (PMF,
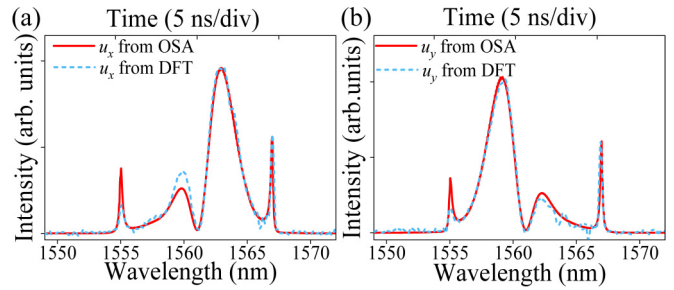

FIG. 12. Comparison between the DFT measured waveforms and time-averaged spectra. (a) u_x component and (b) u_y component. The time-averaged spectra and single-shot spectra are denoted by red (solid) and blue (short dash) curves. OSA, optical spectral analyzer.

PM980-XP), a filmy CNTSA, a polarization controller, and a polarization-insensitive isolator. The DVASM operation is realized at the pump power of ∼60 mW. The pigtails of these fiber components are SMFs (1060-XP) with a total length of 5.25 m. The dispersion parameters D for the YDF, SMF, and PMF are about −43, −41, and −46 ps/(nm km), respectively. The total dispersion and length of the YDF laser are +0.189 ps² and 7.9 m, respectively. The beat lengths of PMF and other fibers are ∼2.4 mm and ∼1 m, respectively.

Corresponding simulations are performed by solving the coupled Ginzburg-Landau equations with the split-step Fourier method [7]. The simulation parameters are set as follows: $c = 3 \times 10^8$ m/s, $\lambda = 1035$ nm. For the SMF, $\Delta n = 0.41 \times 10^{-6}$, $g_0 = 0$, $\beta_2 = 23.3$ ps²/km, $\gamma = 4.7 \times 10^{-3}$ W^{-1} m^{-1}. For the PMF, $\Delta n = 4.12 \times 10^{-4}$, $\gamma = 4.7 \times 10^{-3}$ W^{-1}m^{-1}, $\beta_2 = 26.1$ ps²/km, $\gamma = 4.7 \times 10^{-3}$W^{-1}m^{-1}. For the YDF, $\Delta n = 0.97 \times 10^{-6}$, $g_0 = 7$ m^{-1}, $\beta_2 = 24.4$ ps²/km, $\gamma = 4.7 \times 10^{-3}$W^{-1}m^{-1}. The saturation energy is set as 130 pJ. The saturable absorber is modeled by the transfer function $T = 0.43 - T_0/[1 + P_{(\tau)}/P_{sat}]$, where $T_0 = 0.07$ and $P_{sat} = 8$ W.

[1] J. Denschlag, J. E. Simsarian, D. L. Feder, C. W. Clark, L. A. Collins, J. Cubizolles, L. Deng, E. W. Hagley, K. Helmerson, W. P. Reinhardt, S. L. Rolston, B. I. Schneider, and W. D. Phillips, Generating solitons by phase engineering of a Bose-Einstein condensate, Science **287**, 97 (2000).

[2] N. J. Zabusky and M. D. Kruskal, Interaction of "Solitons" in a Collisionless Plasma and the Recurrence of Initial States, Phys. Rev. Lett. **15**, 240 (1965).

[3] B. Semelin, N. Sánchez, and H. J. de Vega, Self-gravitating fluid dynamics, instabilities, and solitons, Phys. Rev. D **63**, 084005 (2001).

[4] F. M. Knox, W. Forysiak, and N. J. Doran, 10-Gbt/s soliton communication systems over standard fiber at 1.55 μm and the use of dispersion compensation, J. Lightwave Technol. **13**, 1955 (1995).

[5] M. E. Fermann and I. Hartl, Ultrafast fibre lasers, Nat. Photonics **7**, 868 (2013).

[6] Q. Ruan, X. Xiao, J. Zou, H. Wang, S. Fan, T. Li, J. Li, Z. Dong, Z. Cai, and Z. Luo, Visible-wavelength spatiotemporal mode-locked fiber laser delivering 9 ps, 4 nJ pulses at 635 nm, Laser Photonics Rev. **16**, 2100678 (2022).

[7] G. P. Agrawal, *Nonlinear Fiber Optics* (Academic Press, New York, 2001).

[8] D. Y. Tang, L. M. Zhao, B. Zhao, and A. Q. Liu, Mechanism of multisoliton formation and soliton energy quantization in passively mode-locked fiber lasers, Phys. Rev. A **72**, 043816 (2005).

[9] S. Chouli and P. Grelu, Rains of solitons in a fiber laser, Opt. Express **17**, 11776 (2009).

[10] W. W. Hsiang, C. H. Chang, C. P. Cheng, and Y. Lai, Passive synchronization between a self-similar pulse and a bound-soliton bunch in a two-color mode-locked fiber laser, Opt. Lett. **34**, 1967 (2009).

[11] W. He, M. Pang, C. R. Menyuk, and P. St. J. Russell, Sub-100-fs 1.87 GHz mode-locked fiber laser using stretched-soliton effects, Optica **3**, 1366 (2016).

[12] M. Stratmann, T. Pagel, and F. Mitschke, Experimental Observation of Temporal Soliton Molecules, Phys. Rev. Lett. **95**, 143902 (2005).

[13] P. Grelu, F. Belhache, F. Gutty, and J. M. Soto-Crespo, Phase-locked soliton pairs in a stretched-pulse fiber laser, Opt. Lett. **27**, 966 (2002).

[14] B. A. Malomed, Bound solitons in the nonlinear Schrödinger–Ginzburg-Landau equation, Phys. Rev. A **44**, 6954 (1991).

[15] N. N. Akhmediev, A. Ankiewicz, and J. M. Soto-Crespo, Multisoliton Solutions of the Complex Ginzburg-Landau Equation, Phys. Rev. Lett. **79**, 4047 (1997).

[16] J. Peng, Z. Zhao, S. Boscolo, C. Finot, S. Sugavanam, D. V. Churkin, and H. Zeng, Breather molecular complexes in a passively mode-locked fiber laser, Laser Photonics Rev. **15**, 2000132 (2021).

[17] V. Tsatourian, S. V. Sergeyev, C. Mou, A. Rozhin, V. Mikhailov, B. Rabin, P. S. Westbrook, and S. K. Turitsyn, Polarisation dynamics of vector soliton molecules in mode locked fibre laser, Sci. Rep. **3**, 3154 (2013).

[18] Y. Du and X. Shu, Molecular and vectorial properties of the vector soliton molecules in anomalous-dispersion fiber lasers, Opt. Express **25**, 28035 (2017).

[19] A. Maître, G. Lerario, A. Medeiros, F. Claude, Q. Glorieux, E. Giacobino, S. Pigeon, and A. Bramati, Dark-Soliton Molecules in an Exciton-Polariton Superfluid, Phys. Rev. X **10**, 041028 (2020).

[20] W. Weng, R. Bouchand, E. Lucas, E. Obrzud, T. Herr, and T. J. Kippenberg, Heteronuclear soliton molecules in optical microresonators, Nat. Commun. **11**, 2402 (2020).

[21] S. T. Cundiff, B. C. Collings, N. N. Akhmediev, J. M. Soto-Crespo, K. Bergman, and W. H. Knox, Observation of Polarization-Locked Vector Solitons in an Optical Fiber, Phys. Rev. Lett. **82**, 3988 (1999).

[22] K. Nithyanandan, R. V. J. Raja, K. Porsezian, and B. Kalithasan, Modulational instability with higher-order dispersion and walk-off in Kerr media with cross-phase modulation, Phys. Rev. A **86**, 023827 (2012).

[23] C. R. Menyuk, Stability of solitons in birefringent optical fibers. I: Equal propagation amplitudes, Opt. Lett. **12**, 614 (1987).

[24] Y. Luo, J. Cheng, B. Liu, Q. Sun, L. Li, S. Fu, D. Tang, L. Zhao, and D. Liu, Group-velocity-locked vector soliton molecules in fiber lasers, Sci. Rep. **7**, 2369 (2017).

[25] M. Han, S. Zhang, X. Li, H. Zhang, H. Yang, and T. Yuan, Polarization dynamic patterns of vector solitons in a graphene mode-locked fiber laser, Opt. Express **23**, 2424 (2015).

[26] A. Hause, H. Hartwig, M. Böhm, and F. Mitschke, Binding mechanism of temporal soliton molecules, Phys. Rev. A **78**, 063817 (2008).

[27] Z. Q. Wang, K. Nithyanandan, A. Coillet, P. Tchofo-Dinda, and P. Grelu, Optical soliton molecular complexes in a passively mode-locked fibre laser, Nat. Commun. **10**, 830 (2019).

[28] D. Tang, W. S. Man, H. Tam, and P. D. Drummond, Observation of bound states of solitons in a passively mode-locked fiber laser, Phys. Rev. A **64**, 033814 (2001).

[29] M. Anderson, Y. Wang, F. Leo, S. Coen, M. Erkintalo, and S. G. Murdoch, Coexistence of Multiple Nonlinear States in a Tristable Passive Kerr Resonator, Phys. Rev. X **7**, 031031 (2017).

[30] A. U. Nielsen, B. Garbin, S. Coen, S. G. Murdoch, and M. Erkintalo, Coexistence and Interactions between Nonlinear States with Different Polarizations in a Monochromatically Driven Passive Kerr Resonator, Phys. Rev. Lett. **123**, 013902 (2019).

[31] F. Copie, M. T. M. Woodley, L. Del Bino, J. M. Silver, S. Zhang, and P. Del'Haye, Interplay of Polarization and Time-Reversal Symmetry Breaking in Synchronously Pumped Ring Resonators, Phys. Rev. Lett. **122**, 013905 (2019).

[32] G. Xu, A. U. Nielsen, B. Garbin, L. Hill, G. L. Oppo, J. Fatome, S. G. Murdoch, S. Coen, and M. Erkintalo, Spontaneous symmetry breaking of dissipative optical solitons in a two-component Kerr resonator, Nat. Commun. **12**, 4023 (2021).

[33] K. Krupa, K. Nithyanandan, U. Andral, P. Tchofo-Dinda, and P. Grelu, Real-Time Observation of Internal Motion within Ultrafast Dissipative Optical Soliton Molecules, Phys. Rev. Lett. **118**, 243901 (2017).

[34] J. Igbonacho, K. Nithyanandan, K. Krupa, P. T. Dinda, P. Grelu, and A. B. Moubissi, Dynamics of distorted and undistorted soliton molecules in a mode-locked fiber laser, Phys. Rev. A **99**, 063824 (2019).

[35] D. Mao, Z. He, Q. Gao, C. Zeng, L. Yun, Y. Du, H. Lu, Z. Sun, and J. Zhao, Birefringence-managed normal-dispersion fiber laser delivering energy-tunable chirp-free solitons, Ultrafast Sci. **2022**, 9760631 (2022).

[36] D. Mao, Z. He, Y. Zhang, Y. Du, C. Zeng, L. Yun, Z. Luo, T. Li, Z. Sun, and J. Zhao, Phase-matching-induced near-chirp-free solitons in normal-dispersion fiber lasers, Light Sci. Appl. **11**, 25 (2022).

[37] K. Tamura, C. R. Doerr, H. A. Haus, and E. P. Ippen, Soliton fiber ring laser stabilization and tuning with a broad intracavity filter, IEEE Photonics Technol. Lett. **6**, 697 (1994).

[38] A. Komarov, F. Amrani, A. Dmitriev, K. Komarov, D. Meshcheriakov, and F. Sanchez, Dispersive-wave mechanism of interaction between ultrashort pulses in passive mode-locked fiber lasers, Phys. Rev. A **85**, 013802 (2012).

[39] Z. Li, Y. Xu, S. Coen, S. G. Murdoch, and M. Erkintalo, Experimental observations of bright dissipative cavity solitons and their collapsed snaking in a Kerr resonator with normal dispersion driving, Optica **7**, 1195 (2020).

[40] N. N. Akhmediev, A. V. Buryak, J. M. Soto-Crespo, and D. R. Andersen, Phase-locked stationary soliton states in birefringent nonlinear optical fibers, J. Opt. Soc. Am. B **12**, 434 (1995).

[41] D. Mao, X. Liu, and H. Lu, Observation of pulse trapping in a near-zero dispersion regime, Opt. Lett. **37**, 2619 (2012).

[42] K. Goda and B. Jalali, Dispersive Fourier transformation for fast continuous single-shot measurements, Nat. Photonics **7**, 102 (2013).

[43] G. Herink, F. Kurtz, B. Jalali, D. R. Solli, and C. Ropers, Real-time spectral interferometry probes the internal dynamics of femtosecond soliton molecules, Science **356**, 50 (2017).

[44] M. Liu, Z. W. Wei, H. Li, T. J. Li, A. P. Luo, W. C. Xu, and Z. C. Luo, Visualizing the "invisible" soliton pulsation in an ultrafast laser, Laser Photonics Rev. **14**, 1900317 (2020).

[45] Y. Li, Y. Cao, L. Gao, L. Huang, H. Han, I. P. Ikechukwu, and T. Zhu, Fast Spectral Characterization of Optical Passive Devices Based on Dissipative Soliton Fiber Laser Assisted Dispersive Fourier Transform, Phys. Rev. Appl. **14**, 024074 (2020).

[46] F. Kurtz, C. Ropers, and G. Herink, Resonant excitation and all-optical switching of femtosecond soliton molecules, Nat. Photonics **14**, 9 (2019).

[47] N. Akhmediev, J. M. Soto-Crespo, and P. Grelu, Vibrating and shaking soliton pairs in dissipative systems, Phys. Lett. A **364**, 413 (2007).